Mechanochemical Synthesis

CrossMark

Cations size mismatch versus bonding characteristics: synthesis, structure and oxygen ion conducting properties of pyrochlore-type lanthanide hafnates

Nayeli M. Cepeda-Sánchez[1], José A. Díaz-Guillén[2], Miroslaw Maczka[3] ⓘ, Ulises Amador[4] ⓘ, and Antonio F. Fuentes[1,*] ⓘ

[1] *Cinvestav Unidad Saltillo, 25900 Ramos Arizpe, Coahuila, Mexico*

[2] *División de Estudios de Posgrado e Investigación, Instituto Tecnológico de Saltillo, 25280 Saltillo, Coahuila, Mexico*

[3] *Institute of Low Temperature and Structure Research, Polish Academy of Sciences, 50-950 Wrocław 2, Poland*

[4] *Departamento de Química y Bioquímica, Facultad de Farmacia, Universidad San Pablo-CEU, 28668, Boadilla del Monte, Madrid, Spain*

ABSTRACT

This work describes the synthesis, structural characterization and electrical properties of solid solutions with the general formula $Gd_2Hf_{2-x}B_xO_7$, where $B = Ti^{4+}$, Sn^{4+} and Zr^{4+}. All samples were successfully prepared in $\sim$ 30 h, via a mechanochemical reaction in a planetary ball mill, using the corresponding elemental oxides as starting chemicals. The XRD and Raman spectroscopy analysis of the title samples revealed that on firing at 1500 °C Hf^{4+} substitution by Sn^{4+} and Ti^{4+} produces better ordered pyrochlore structures and decreases the electrical conductivity of $Gd_2Hf_2O_7$ by more than two orders of magnitude (from 2.7×10^{-4} at 700 °C to 8.71×10^{-7} and 1.12×10^{-6} Sm cm^{-1}, for $Gd_2Sn_2O_7$ and $Gd_2Ti_2O_7$, respectively). By contrast, the $Gd_2Hf_{2-x}Zr_xO_7$ system remains disordered with conductivity increasing by almost an order of magnitude and reaching a value for $Gd_2Zr_2O_7$ of 1.55×10^{-3} Sm cm^{-1} at 700 °C, whereas the activation energy for oxygen migration decreases in both, the Sn- and Ti-containing systems, and increases slightly in the Zr-containing solid solution. These changes cannot be only explained when taking into account the cations size ratio criteria; the covalency of the <B–O> metal bond plays also a key role in determining the structural characteristics and electrical properties of the title three systems.

Address correspondence to E-mail: fuentesaf@live.com

Springer

Introduction

The *pyrochlore* structure is widely adopted by synthetic $A_2B_2O_7$ multicomponent oxides because it can accommodate a broad range of cation combinations, mixed site populations, and vacancies [1]. Thus, the *A*-site can be occupied by a great variety of large cations (r_A = 0.9–1.2 Å) in different oxidation states such as Bi^{3+}, Pb^{2+} or Ln^{3+} (lanthanide ions) to name a few. The *B*-site might host almost any medium size ($\sim$ 0.6–0.75 Å) and positively charged ion capable of adopting a sixfold coordination, such as Sn^{4+}, Zr^{4+}, Hf^{4+}, Ti^{4+}, Nb^{5+}, or Ir^{4+}. Some oxygen- and cation-deficient pyrochlores show gross deviations from the ideal $A_2B_2O_7$ stoichiometry and yet remain thermodynamically stable even without a significant distortion of the ideal isometric unit cell [2–4]. Coupled to such interesting structural and compositional features, pyrochlore oxides display a rather unique set of exciting physical and chemical properties. Thus, pyrochlores electrochemical properties span from metallic or even superconducting behavior, to fast ion and mixed ionic-electronic conduction, semiconductors and insulators [5–8]. Some of these properties are mediated by subtle electronic features or by the presence of structural defects and disorder, which occur easily in this family of oxides. Moreover, the pyrochlore structure offers a unique playground to examine the interplay between chemical composition, defect chemistry and properties.

This contribution addresses some of these issues by analyzing the effect of isovalent substitutions on the structure and oxygen ion conducting properties of a pyrochlore-type hafnate, $Gd_2Hf_2O_7$. Pyrochlore-type lanthanide-containing oxides $Ln_2B_2O_7$, where B is a tetravalent cation, have attracted a great deal of interest in recent years for both, fundamental science

and practical applications in fields such as energy conversion and storage, thermal insulation or even, immobilization of high-level radioactive waste [9–11]. We have recently engaged in a study of the synthesis, structural characteristics and physicochemical properties of otherwise, insufficiently studied lanthanide hafnates [12–15], and this work is part of this effort.

The *pyrochlore* structure might be considered a *fluorite*-related superstructure [1]. The *fluorite* structure [S.G. = $Fm\bar{3}m$ (#225)] can be described as a face-centered cubic (*fcc*) array of cations in which all the available tetrahedral interstices are filled with anions. Although retaining the *fcc* array, cations in the *pyrochlore* structure [S.G. = $Fd\bar{3}m$ (#227)] are ordered on two nonequivalent sites. Furthermore, anions are also located as in *fluorites*, in the tetrahedral interstices of the cation framework although they are all no longer equivalent, but occupy two symmetry-independent positions. Both structures are compared in Table 1 and in Fig. 1.

Different attempts have been made in the literature to rationalize the formation and stability of the *pyrochlore* structure, in terms of simple geometrical requirements such as the cations radii and their size mismatch [1, 16–18]. Thus, the radius ratio constraints in $A_2B_2O_7$ oxides result in the formation of the *pyrochlore* structure when $1.46 \leq r_A/r_B \leq 1.78$. Outside this range, the size mismatch favors different structure types such as perovskite-related monoclinic layered structures ($r_A/r_B > 1.78$) and anion deficient *fluorite* structures ($r_A/r_B < 1.46$). However, geometric and electrostatic criteria only are not enough to fully explain the formation and stability of *pyrochlore*-type phases. Additional factors, such as bonding character, processing conditions, and thermal history, play also an important role in stabilizing/destabilizing the

Table 1 The fluorite and pyrochlore structures

	Fluorite	Pyrochlore
Formula unit	BO_2	$A_2B_2O_7$
Space group	$Fm\bar{3}m$ (225)	$Fd\bar{3}m$ (227)
Cell dimensions	$a \sim$ (4–8) Å	$a \sim$ (10–11) Å
Cell content	4 *formula units*	8 *formula units*
Wyckoff sites cation sublattice	4c (0 0 0) (*c.n.* = 8)	16c (0 0 0) (*c.n.* = 8)
		16d (1/2 1/2 1/2) (*c.n.* = 6)
Wyckoff sites anion sublattice	8c (1/4 1/4 1/4) (*c.n.* = 4)	48f (x 1/8 1/8) (*c.n.* = 4)
		8a (1/8 1/8 1/8) (*c.n.* = 4)

Origin choice 2 in space group 227; *c.n.* = coordination number

Figure 1 A comparison between the fluorite (left) and pyrochlore (right) structures. Top: A fluorite-type unit cell and 1/8th of a pyrochlore-type unit cell. Bottom: Projection of 8 fluorite-type unit cells and of a single pyrochlore-type unit cell. Blue and light blue spheres represent cations, whereas yellow and red spheres represent anions.
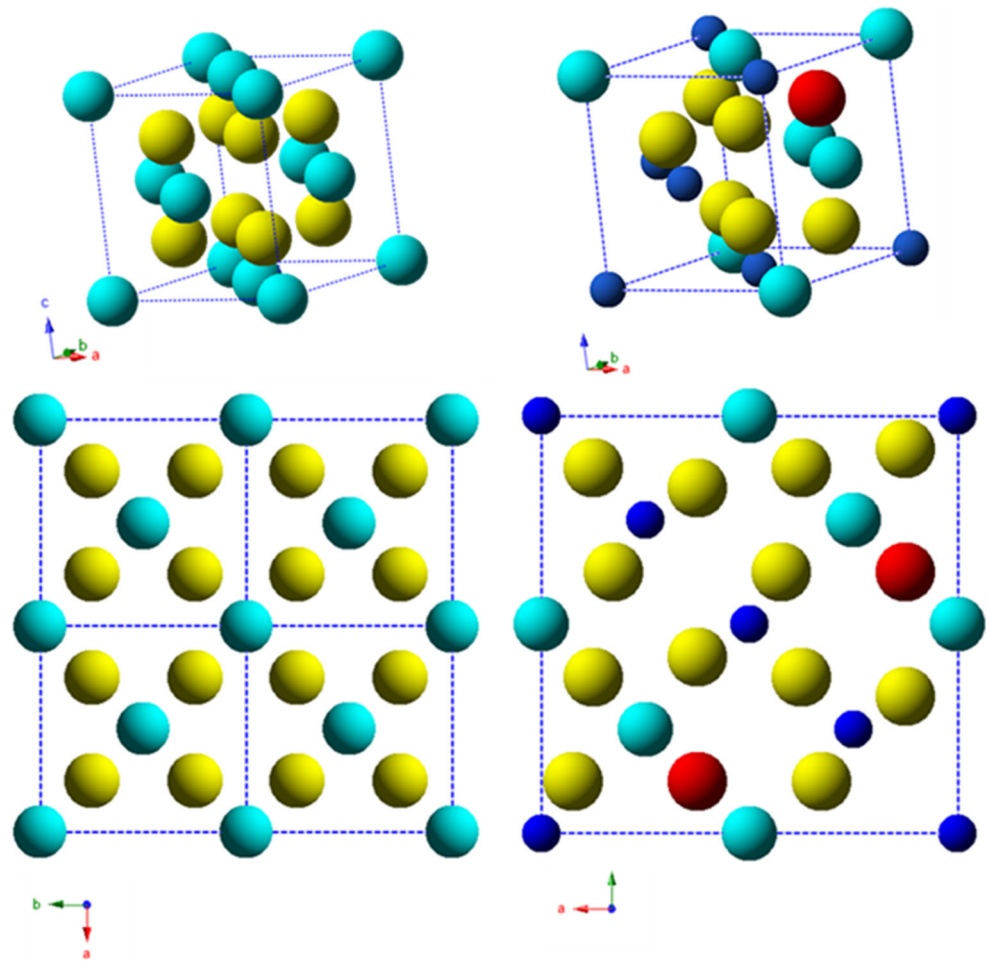
pyrochlore structure and, indeed, in determining its properties.

The use of mechanical energy to stimulate physical and chemical processes in the solid state, the so-called mechanochemical methods (MM), has attracted great deal of interest in materials science for different reasons [19–22]. First, they are simple to implement and capable of providing large volumes of the target material in a cost-effective manner. Furthermore, as far-from-equilibrium processing techniques, MM frequently yield highly defective and metastable phases; additional processing allows obtaining fairly stable intermediate states with intriguing and potentially interesting characteristics, which are inaccessible by more conventional processing techniques. Having in mind the extremely refractory nature of lanthanide hafnates and the importance of some structural defects on transport properties of ion conducting materials, we selected this powder processing method, to obtain all the samples analyzed in this work.

Experimental

The samples preparation and characterization procedure followed in this work has been described in detail elsewhere [12–14]. Different compositions in the three $Gd_2(Hf_{2-x}B_x)_2O_7$ systems ($B = Ti^{4+}$, Sn^{4+} and Zr^{4+}; $x = 0, 0.4, 0.8, 1.2, 1.6$ and 2) were prepared by dry milling at room temperature, stoichiometric mixtures of the corresponding high purity ($\geq 99\%$) elemental oxides, *baddeleyite*-type HfO_2 and ZrO_2, *anatase*-TiO_2, *cassiterite*-SnO_2, and C-Gd_2O_3. Milling was carried out in a Retsch PM400 planetary ball mill (rotation speed = 350 rpm), using YPSZ (5 wt% Y_2O_3) containers (volume = 125 ml; sample size = 20 g), and grinding media (20 mm $\varnothing$; balls-to-powder mass ratio = 10:1). The evolution of selected reacting mixtures with milling time was followed by using X-ray diffraction (XRD). Mechanochemical reactions were considered completed when no traces of the starting chemicals were observed by this technique. As-prepared samples were subjected to

post-milling thermal treatments at 1500 °C and analyzed as described below. The structural and microstructural features were obtained from precise diffraction data collected by using a Bruker D8 high-resolution X-ray powder diffractometer equipped with a Ge(111) primary monochromator ($CuK_{\alpha 1}$ radiation, $\lambda = 1.5406$ Å), and a LynxEye® rapid detector. The angular range, step size and counting times were adjusted to obtain good resolution (the step size should be, at least, 1/10th of the FWHMs), and statistics. The instrumental contribution to peak broadening was evaluated by using NIST LaB_6 standard reference material (SRM 660a). The structural refinements were undertaken by using the Rietveld method and the FullProf program [23], to determine the lattice parameter, atomic positions (O in x_{48f}) and the isotropic thermal factors (Debye–Waller); the chemical composition was included as constraint during the refinements since no additional phases were ever detected. Furthermore, the distribution of metal ions was allowed to move between the 16d and 16c site although always having in mind that smaller ions would prefer to sit at the 16d site, and correspondingly, larger ions would tend to occupy the 16c site. The samples microstructure was determined by the phenomenological approach described in detail elsewhere [24–27]. The oxygen array in our structural refinements is assumed to be ordered, as in the ideal pyrochlore structure. Raman spectra were collected in a Horiba Scientific LabRAM HR Evolution NIR spectrometer, equipped with an Olympus BX41 confocal microscope, a solid-state blue excitation laser (473 nm) and a liquid N_2-cooled CCD detector.

The electrical characterization was carried out in pressed powders (applied pressure = 7 Tons cm^{-2}; pellets size = 10 mm diameter and $\sim$ 1 mm thickness) sintered at 1500 °C for 12 h (heating/cooling rate = 5 °C min^{-1}). Pellets density was determined by using the Archimedes method and deionized water as the immersion medium; measurements were carried out in an Ohaus Discovery DV314C analytical balance ($\pm$ 0.1 mg), equipped with a density determination accessory (P/N 77402-00). AC impedance measurements were carried out in air, as a function of frequency (100 Hz to 1 MHz) and temperature (250–700 °C), using a Solartron 1260 Frequency Response Analyzer and a ProboStat® sample holder system. Electrodes for impedance spectroscopy were made by coating opposite faces of the pellets, with conductive Pt paste and firing in air at 800 °C to eliminate organic components and harden the Pt residue.

Results and discussion

Synthesis

Figure 2 presents selected XRD patterns, collected at different stages of the synthesis of the $Gd_2Hf_{2-x}Sn_xO_7$ system. The synthesis of the $Gd_2Hf_{2-x}Ti_xO_7$ and $Gd_2Hf_{2-x}Zr_xO_7$ systems were presented elsewhere and would be referred here only for comparison purposes [13, 14]. Figure 2a shows the XRD pattern of a Gd_2O_3:HfO_2:SnO_2 reacting mixture (1:1.6:0.4 molar ratio), selected as representative of the series. Numbers in parenthesis are the Miller indexes of the most intense reflections, characteristic of the three starting chemicals: i.e., MH = baddeleyite m-HfO_2; CG = C-Gd_2O_3 and T = cassiterite-SnO_2; vertical lines at the bottom part of this figure represent the Bragg peaks of these oxides, as reported in the ICDD®. Figure 2b shows the evolution of this mixture with milling time, whereas Fig. 2c shows the XRD patterns of all compositions that were prepared in the $Gd_2Hf_{2-x}Sn_xO_7$ system, as taken out of the mill (decreasing Hf^{4+} content from top to bottom); dashed lines in Fig. 2b, c are provided as a guide to the eye. As observed in 2b, diffraction lines belonging to C-Gd_2O_3, which are the most intense in the XRD pattern of the starting mixture (Fig. 2a), have almost disappeared after milling for only 1 h (e.g., the (440) line at $\sim$ 47.5° (2θ) shows more than 80% reduced intensity), whereas characteristic lines of m-HfO_2 [e.g., (111) line at 31.6°, 2θ] and SnO_2 [e.g., (110) line at 26.6°, 2θ] are still very much evident, after milling for 6 or even 9 h. The rapid weakening and apparent disappearance of C-Gd_2O_3 diffraction lines from the pattern in such a short milling time is probably due to its polymorphic transformation to monoclinic B-Gd_2O_3, which might be activated by temperature ($\sim$ 1100 °C), but also by high-energy milling [28]; in our mixture, the most intense reflections characteristic of B-Gd_2O_3, which are found between 28 and 33° (2θ), is obscured between the two strongest lines of m-HfO_2, the (− 111) and (111) lines.

By contrast, no evidence was ever found by XRD of an m- to t- or c-HfO_2 (tetragonal or cubic) polymorphic transformation, probably because much higher
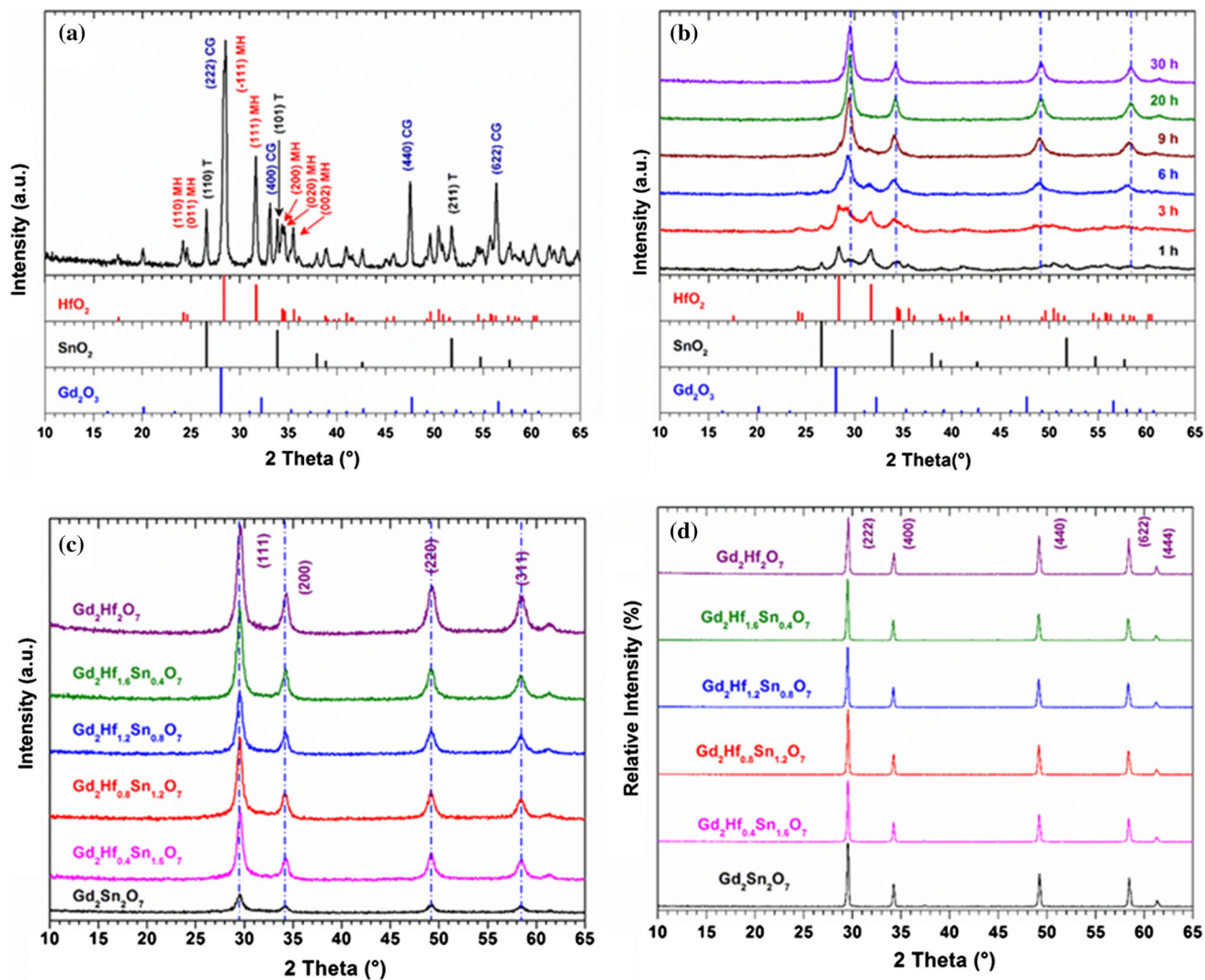
Figure 2 **a** XRD pattern of a Gd_2O_3:HfO_2:SnO_2 starting mixture (1:1.6:0.4 molar ratio); **b** Evolution of the same mixture with milling time; **c** XRD patterns of all compositions prepared in this work as taken out of the mill; **d** XRD patterns of the same compositions after firing them at 1500 °C.

energy is required in this case (transformation temperatures to *t*- or *c*-HfO_2, are ∼ 1720 °C and ∼ 2600 °C, respectively). Although these HfO_2 higher symmetry forms might be also stabilized at lower temperatures by the incorporation of lanthanide ions such as Gd^{3+}, that does not happen apparently in our reacting mixtures. The formation of a reaction product and therefore the existence of a mechanochemical reaction becomes clear after milling for 6 h with new strong reflections emerging at ∼ 30°, ∼ 34°, ∼ 49° and ∼ 58° (2θ); this new set of reflections becomes narrower and more intense, with increasing milling time. Finally, the XRD pattern obtained after milling for 30 h is similar to that characteristic of a fluorite lattice, with no evidence of the starting

chemicals, additional phases or any other impurity suggesting then, a complete reaction at this point. Very broad diffraction peaks as those observed in these patterns are characteristic of materials prepared by mechanosynthesis because of the small crystallite size and the high density of structural defects induced by milling. These results highlight the advantages of using mechanochemical methods to obtain extremely refractory compounds such as these lanthanide hafnates, which require very high temperatures (typically ≥ 1600 °C) and long and repeated firing cycles, when prepared by the traditional ceramic method. According to Fig. 2c, all the compositions prepared in this system seem to be either highly disordered pyrochlore or fluorite-like

Table 2 The r_A/r_B values calculated for the end limits of the three solid solutions studied in this work

	r_B (c.n. = 6), Å		r_{Gd}/r_B
Ti^{4+}	0.605	$Gd_2Ti_2O_7$	1.740
Sn^{4+}	0.690	$Gd_2Sn_2O_7$	1.526
Hf^{4+}	0.710	$Gd_2Hf_2O_7$	1.483
Zr^{4+}	0.720	$Gd_2Zr_2O_7$	1.462

r_{Gd} (c.n. =8)= 1.053 Å

materials since none of the superlattice reflections characterizing the long-range ordering of cations, anions and vacancies in the pyrochlore structure [29], are evident by XRD: e.g., the (111), (311), (331) and (511) lines at, respectively, $\sim 15°$, $\sim 29°$, $\sim 39°$ and $\sim 46°$ (2θ). Therefore, Miller indexes shown in Fig. 2c are characteristic of fluorite-like phases, whereas Fig. 2d shows the XRD patterns of the same six compositions, after firing them at 1500 °C. As we have shown before in previous works [13, 30], $Gd_2Hf_2O_7$- or $Gd_2Zr_2O_7$-based powders prepared by mechanosynthesis present a fluorite-like structure; depending on the firing temperature, post-milling thermal treatments facilitate the relaxation (at least partially) of mechanically induced defects and the transformation to more ordered pyrochlore-type structures, in a top-down approach to the

corresponding equilibrium phase diagrams. Although the XRD patterns shown in Fig. 2d are apparently similar to those of fluorite-like phases, a deeper inspection using precise X-ray diffraction data collected with a high-resolution diffractometer showed a different picture.

Structural refinement by the Rietveld method

Table 2 presents the r_A/r_B values for the end limit compositions of the three systems analyzed in this work, calculated using the ionic radii values given by Shannon [31]. Therefore, according to the size mismatch criteria, Hf^{4+} substitution by Ti^{4+} and to a lesser extent by Sn^{4+} should increase the stability of the pyrochlore structure and produce better ordered phases (increasing r_A/r_B), whereas introducing Zr^{4+} instead of Hf^{4+} should barely affect the degree of structural disorder in $Gd_2Hf_2O_7$. Moreover, all intermediate compositions should also crystallize on the pyrochlore structure; Tables 3, 4 and 5 show a summary of the results obtained by the Rietveld method in the three systems, $Gd_2Hf_{2-x}Sn_xO_7$, $Gd_2Hf_{2-x}Zr_xO_7$ and $Gd_2Hf_{2-x}Ti_xO_7$; those of the $Gd_2Hf_{2-x}Ti_xO_7$ solid solution were already discussed in a previous paper [13] and are included here only for

Table 3 Structural parameters for mechanochemically prepared $Gd_2(Hf_{2-x}Sn_x)O_7$ powders, after firing at 1500 °C for 12 h as obtained from their XRD patterns

Sample composition	(a) $x = 0$	$x = 0.4$	$x = 0.8$	$x = 1.2$	$x = 1.6$	$x = 2.0$
a (Å)	10.49404(2)	10.48413(1)	10.48469(1)	10.48195(1)	10.47681(1)	10.46776(1)
Gd/Sn/Hf at 16c (0 0 0)	1.41(2)/–/ 0.59(2)	1.53(2)/–/ 0.47(2)	1.68(2)/–/ 0.32(2)	1.79(2)/–/ 0.21(2)	1.90(2)/–/ 0.10(2)	2.00/–/–
Gd/Sn/Hf at 16d (1/2 1/2 1/2)	0.59(2)/–/ 1.41(2)	0.47(2)/0.40/ 1.13(2)	0.32(2)/0.80/ 0.88(2)	0.21(2)/1.20/ 0.59(2)	0.10(2)/1.60/ 0.30(2)	–/2.0/–
O(1) at 48f (x 1/8 1/8)	1	1	1	1	1	1
x_{48f}	0.4036(5)	0.4889(6)	0.4105(6)	0.4115(6)	0.4130(5)	0.4138(6)
O(2) at 8a (1/8 1/8 1/8)	1	1	1	1	1	1
R_B (%)	5.57	2.24	3.94	1.92	1.74	2.44
R_{wp} (%)	2.50	3.36	3.32	3.28	3.00	3.18
R_{exp} (%)	1.24	2.97	2.84	3.01	2.62	2.65
χ^2	4.06	1.29	1.36	1.19	1.31	1.44
(b) $<D_{iso}>$ (Å)	397(13)	736(17)	1688(570)	1852(281)	442(61)	698(13)
(c) e_{rms}	$6.1(7) \times 10^{-5}$	$8.20(3) \times 10^{-4}$	No stress	No stress	No stress	$9.02(7) \times 10^{-4}$

(a) All the samples present a pyrochlore-like structure with S.G. $Fd\bar{3}m$ (#227). The respective occupations are those given by the chemical formula. Cell content is obtained as the site multiplicity times the occupancy; $Z = 8$

(b) $<D_{iso}>$ is the average domain diameter, assuming spherical shape

(c) $<e_{rms}>$ is the mean square strain in the structure

Table 4 Structural parameters for mechanochemically prepared $Gd_2(Hf_{2-x}Zr_x)O_7$ powders, after firing them at 1500 °C for 12 h, as obtained from their XRD patterns

Sample composition	[a] $x = 0$	$x = 0.4$	$x = 0.8$	$x = 1.2$	$x = 1.6$	$x = 2.0$
a (Å)	10.49427(2)	10.50952(2)	10.51113(1)	10.50753(2)	10.48827(2)	10.49035(2)
Gd/Zr/Hf at 16c (0 0 0)	1.30(2)/–/0.70(2)	1.713(3)/–/0.287(3)	1.71(3)/–/0.29(3)	1.94(3)/–/0.06(3)	1.95(2)/–/0.05(2)	1.59(2)/0.41(2)/–
Gd/Zr/Hf at 16d (1/2 1/2 1/2)	0.70(2)/–/1.30(2)	0.50(4)/0.4/1.10(4)	0.29(3)/0.8/0.91(3)	0.06(3)/1.2/0.74(3)	0.05(2)/1.6/0.35(2)	0.41(2)/1.59(2)–
O(1) at 48f (x 1/8 1/8)	1	1	1	1	1	1
x_{48f}	0.4030(6)	0.3964(7)	0.4008(6)	0.4039(6)	0.4067(7)	0.4018(6)
O(2) at 8a (1/8 1/8 1/8)	1	1	1	1	1	1
R_B (%)	5.72	5.41	5.04	6.23	6.85	5.53
R_{wp} (%)	2.51	2.11	2.06	2.58	3.64	2.10
R_{exp} (%)	1.24	1.47	1.20	1.52	1.43	1.36
χ^2	4.08	2.07	2.94	2.86	6.46	2.39
[b] $<D_{iso}>$ (Å)	397(13)	Very large	Very large	5484(607)	Very large	3120(150)
[c] e_{rms}	$6.1(7) \times 10^{-5}$	No stress	No stress	$2.05(1) \times 10^{-4}$	No stress	$1.16(2) \times 10^{-4}$

(a) All the samples present a pyrochlore-like structure with S.G. $Fd\bar{3}m$ (#227). The respective occupations are those given by the chemical formula. Cell content is obtained as the site multiplicity times the occupancy; Z = 8

(b) $<D_{iso}>$ is the average domain diameter, assuming spherical shape

(c) $<e_{rms}>$ is the mean square strain in the structure

Table 5 Structural parameters for mechanochemically prepared $Gd_2(Hf_{2-x}Ti_x)O_7$ powders, after firing at 1500 °C for 12 h as obtained from their XRD patterns

Sample composition	[a] $x = 0$	$x = 0.4$	$x = 0.8$	$x = 1.2$	$x = 1.6$	$x = 2.0$
a (Å)	10.49404(2)	10.42064(3)	10.36858(1)	10.31717(2)	10.36858(1)	10.2092(6)
Gd/Ti/Hf at 16c (0 0 0)	1.41(2)/–/0.59(2)	1.76(2)/–/0.24(2)	1.680(1)/0.080(3)/0.249(1)	1.767(1)/0.040(2)/0.194(1)	1.761(1)/0.079(2)/0.161(1)	1.961(5)/0.084(5)/–
Gd/Ti/Hf at 16d (1/2 1/2 1/2)	0.59(2)/–/1.41(2)	0.24(2)/0.40/1.36(2)	0.325(1)/0.720(3)/0.956(1)	0.233(1)/1.160(2)/0.606(1)	0.239(1)/1.521(2)/0.239(1)	0.084(5)/1.961(5)/–
O(1) at 48f (x 1/8 1/8)	1	1	1	1	1	1
x_{48f}	0.4036(5)	0.4085(8)	0.4108(6)	0.41457(7)	0.4178(4)	0.4256(5)
O(2) at 8a (1/8 1/8 1/8)	1	1	1	1	1	1
R_B (%)	5.57	5.67	4.42	5.04	5.42	4.49
R_{wp} (%)	2.50	3.27	2.68	2.83	3.05	2.38
R_{exp} (%)	1.24	1.60	2.04	2.14	1.67	1.86
χ^2	4.06	4.41	1.72	1.74	3.33	1.63
[b] $<D_{iso}>$ (Å)	397(13)	803(14)	2911(68)	Very large	1294(17)	Very large
[c] e_{rms}	$6.1(7) \times 10^{-5}$	$1.6(9) \times 10^{-4}$	$1.3(3) \times 10^{-4}$	No stress	$1.9(4) \times 10^{-4}$	No stress

(a) All the samples present a pyrochlore-like structure with S.G. $Fd\bar{3}m$ (#227). The respective occupations are those given by the chemical formula. Cell content is obtained as the site multiplicity times the occupancy; Z = 8

(b) $<D_{iso}>$ is the average domain diameter, assuming spherical shape

(c) $<e_{rms}>$ is the mean square strain in the structure

comparison purposes. Figure 3 shows the graphical results of fitting two different samples: (a) $Gd_2Hf_{0.4}Zr_{1.6}O_7$ and (b) $Gd_2Hf_{0.4}Zr_{1.6}O_7$.

All patterns were successfully refined to the pyrochlore structure, as expected according to Table 2. However, not all of them show the same degree of

Figure 3 Graphical results of fitting two different samples selected as representatives for the series: **a** $Gd_2Hf_{0.4}Zr_{1.6}O_7$ and **b** $Gd_2Hf_{0.4}Zr_{1.6}O_7$.
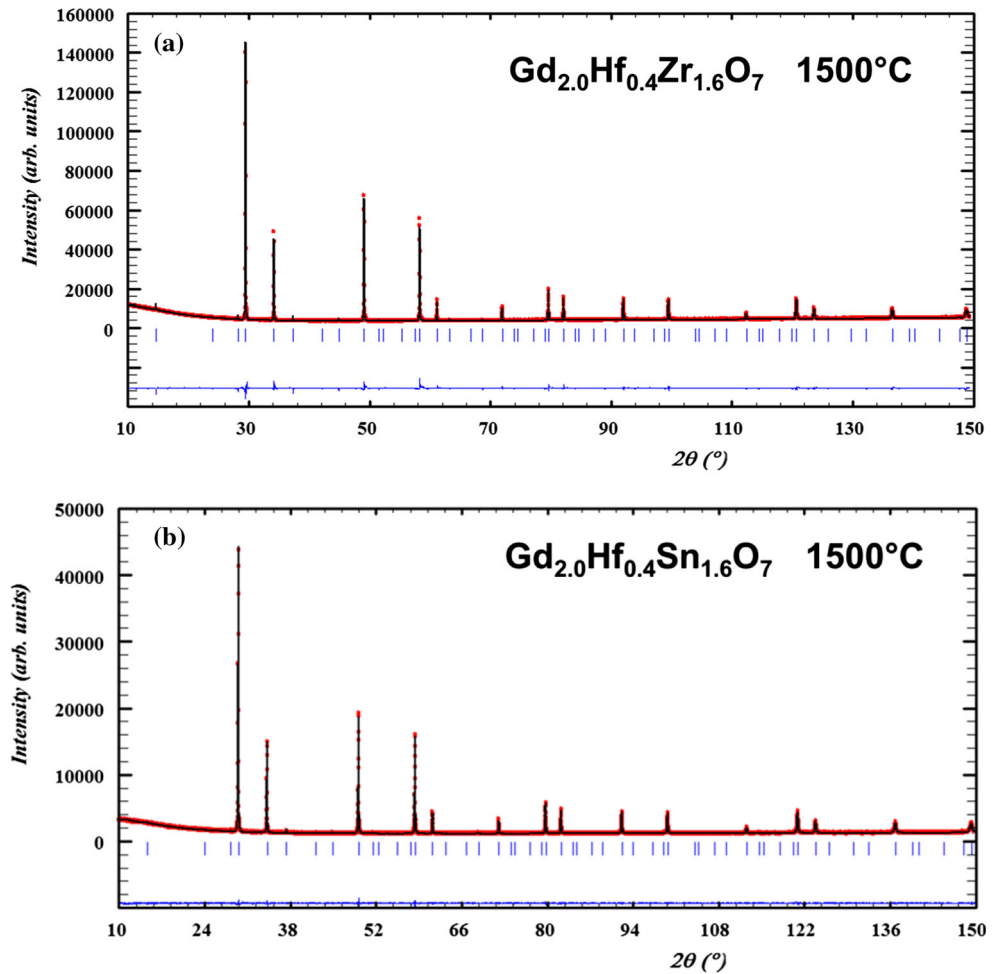
structural disorder. Therefore, as Table 3 shows, the unit cell parameter in the $Gd_2Hf_{2-x}Sn_xO_7$ system hardly changes with increasing Sn^{4+} content, as expected from the small difference in ionic radii between $^{VI}Hf^{4+}$ and $^{VI}Sn^{4+}$, whereas disorder decreases drastically across the entire system, with little cation anti-site disorder present in $Gd_2Sn_2O_7$, i.e., after firing the as-prepared $Gd_2Sn_2O_7$ powders at high temperature, the cation distribution is very close to that expected from the thermodynamic equilibrium configuration, with Gd^{3+} confined to the eightfold coordinated 16c site, and Hf^{4+} and Sn^{4+}, both sharing the sixfold coordinated 16d site. Our results are in agreement with neutron diffraction studies carried out in lanthanide stannates, which have shown no evidence of cation anti-site defects or anion disorder but considerable covalency of the <Sn–O> bond [32]. Even in those Hf-rich compositions showing some cation anti-site defects, the best structural refinement results were obtained when

assuming that Sn^{4+} ions remain at the sixfold coordinated site and allowing both Gd^{3+} and Hf^{4+} to disorder between the 16d and 16c positions. Comparable results have been recently obtained by ^{119}Sn MAS NMR and Sn L_3-edge XANES studies carried out in the $Y_2Sn_{2-x}Zr_xO_7$ system [33], where despite a pyrochlore-to-fluorite phase transition taking place on increasing Zr^{4+} content, Sn^{4+} showed a strong preference to occupy the sixfold coordinated 16d site in the entire system, i.e., its first coordination sphere remains always basically as SnO_6. By contrast, $Gd_2Hf_2O_7$ presents a highly disordered structure even after firing at 1500 °C with almost 30% of all Gd^{3+} atoms occupying the "wrong" sixfold site, whereas an equal number of Hf^{4+} atoms are located at the eightfold coordinated 16c position. As shown in Table 4, this disordered structure is hardly affected when the replacing cation is Zr^{4+}, and the entire system shows a defect pyrochlore structure, with a significant density of cation anti-site defects. A
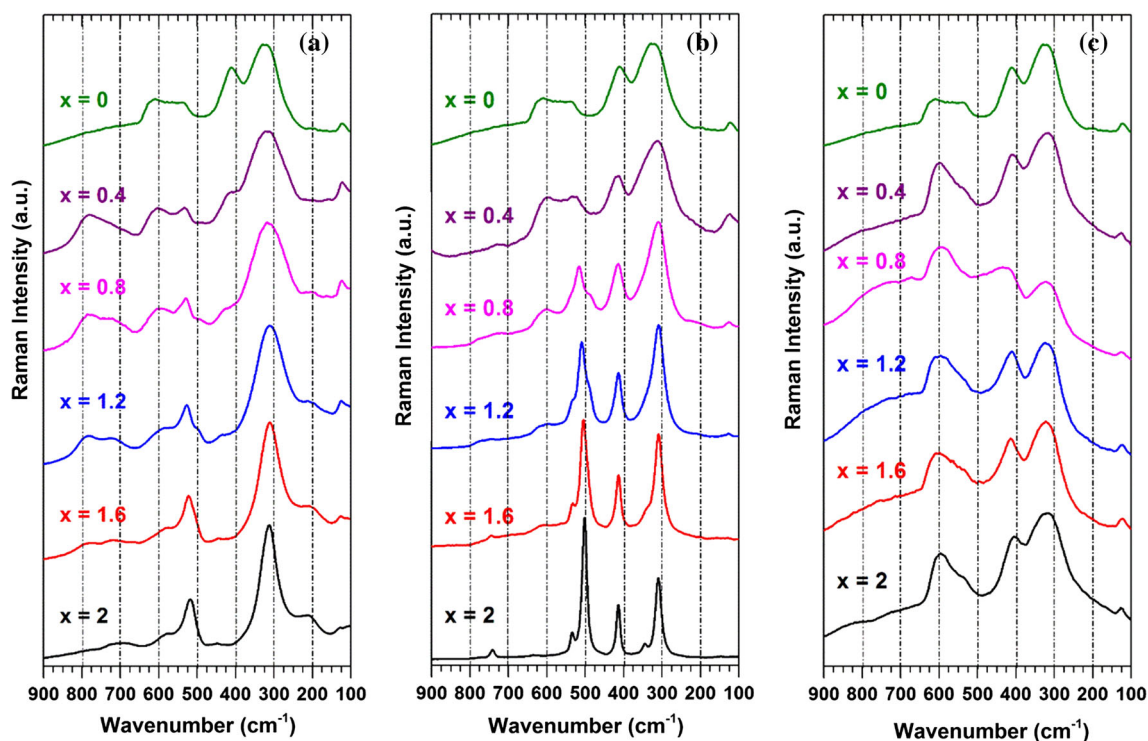
Figure 4 Evolution of the Raman spectra of each of the three series prepared in this work: $Gd_2Hf_{2-x}Ti_xO_7$ (**a**), $Gd_2Hf_{2-x}Sn_xO_7$ (**b**) and $Gd_2Hf_{2-x}Zr_xO_7$ (**c**).

complex cation distribution among the two cation sites is observed, most likely due to the history (mechanical and thermal) of each sample; the only clear point is that Zr^{4+} tends to occupy the sixfold coordination. As the cell parameter of the pyrochlore structure is mostly determined by the size of the BO_6 trigonal antiprism, the average size of the cations located in the 16d sites mainly determines the cell dimensions. In the case of the $Gd_2Hf_{2-x}Zr_xO_7$ series, since Hf^{4+} and Zr^{4+} cations present similar size, the population of large Gd^{3+} determines the unit cell dimension, i.e., higher concentration of cation antisite defects (higher structural disorder) results in larger unit cells.

For the $Gd_2Hf_{2-x}Ti_xO_7$ system due to the small size of Ti^{4+} that ensures a strong tendency to sixfold coordination, the population of Gd^{3+} ions at the 16d-site decreases rapidly on Hf^{4+} substitution and remains below 15% throughout the whole system. Finally, cation distribution in $Gd_2Ti_2O_7$ corresponds to that expected based only in thermodynamic reasons.

The importance of bonding characteristics in pyrochlore disordering has been confirmed by experimental data. Despite of having almost the same

cations size mismatch, the $Gd_2Ti_{2-x}Sn_xO_7$ and $Gd_2Ti_{2-x}Zr_xO_7$ systems show different evolution upon Ti substitution, whereas no significant change in the degree of structural disorder was observed in the Sn-containing system, a high number of defects evolve with increasing Zr content. The higher covalency of the <Sn–O> bonds as compared with <Ti–O> and <Zr–O> has been suggested to explain such differences [9].

Since XRD gives only an averaged structure, we used Raman spectroscopy to obtain more information about the local structure.

Raman spectroscopy

As structural disorder within the pyrochlore structure breaks up its translational symmetry and has a significant impact in the spectra, Raman spectroscopy is frequently used to obtain information about disordering trends in pyrochlore-type systems. It is noteworthy that such disruption allows more phonons to contribute to the optical spectra causing a general broadening of all Raman-active modes on disordering.

Therefore, according to the selection rules, the disordered anion deficient fluorite structure should have only one Raman-active mode of F_{2g} symmetry, with the form of oxygen anions vibrating against the symmetry-fixed cations [34]. By contrast, $A_2B_2O_7$ pyrochlore-type phases should have six Raman-active modes. Five of them (i.e., $A_{1g} + E_g + 3F_{2g}$) are commonly assigned to vibrations of O_{48f} ions, which are bonded to two A and two B cations; the remaining one (F_{2g}), to vibrations of the O_{8a} ions, bonded only to four A cations [34–36]. Specifically, only O_{48f} ions vibrate (predominantly bending) in A_{1g} and E_g modes; furthermore, A_{1g} is directly related to the only free parameter of the pyrochlore crystal structure, the x_{48f} positional parameter. Figure 4 presents the evolution of the Raman spectrum of $Gd_2Hf_2O_7$, when replacing Hf^{4+} by isovalent (a) Ti^{4+} ($Gd_2Hf_{2-x}Ti_xO_7$), (b) Sn^{4+} ($Gd_2Hf_{2-x}Sn_xO_7$) and (c) Zr^{4+} ($Gd_2Hf_{2-x}Zr_xO_7$); to ease the discussion, the top spectrum in (a), (b) and (c) is always that of pristine $Gd_2Hf_2O_7$. As observed in this figure, the spectrum of $Gd_2Hf_2O_7$ (i.e., $x = 0$) is dominated by two strong bands centered at 337 and 412 cm^{-1}. Similar bands have been observed for pyrochlore-type $La_2Hf_2O_7$ and they can be assigned to ($F_{2g} + E_g$) and F_{2g} modes, respectively [37]. As discussed in our previous work [13], the weak band at 543 cm^{-1} can be assigned to the A_{1g} mode, whereas the remaining two F_{2g} modes are located near 602 and 490 cm^{-1}. Worth mentioning is that all bands are very broad and the A_{1g} mode characteristic of the pyrochlore structure is very weak. Since these two features are considered to stem from structural disorder, the Raman spectrum of $Gd_2Hf_2O_7$ is consistent with the highly disordered pyrochlore structure observed by XRD for this compound. Increasing Ti^{4+} content (from top to bottom in Fig. 4a) induces some important changes in the Raman-active bands of $Gd_2Hf_2O_7$. Thus, all bands in the spectra exhibit important shifts with increasing substitution, most of them toward lower wavenumbers (e.g., from 337, 543 and 602 cm^{-1} to 309, 515 and 577 cm^{-1} for $x = 2$, i.e., $Gd_2Ti_2O_7$), although some bands shift also toward higher wavenumbers (e.g., from 412 to 446 cm^{-1}). Furthermore, the band near 490 cm^{-1} is absent in $Gd_2Ti_2O_7$, and those at 446 and 577 cm^{-1}, present a considerable reduction in intensity.

By contrast, the A_{1g} band shows increased intensity with higher Ti^{4+} content; overall, most bands show significant narrowing with increasing level of Hf^{4+}

substitution. These two later characteristics have been related to higher structural ordering [13, 34, 38], and they suggest that doping with Ti^{4+} leads to a considerable growth of the pyrochlore-like domains. Note that the spectrum of $Gd_2Hf_2O_7$ shows additional very broad bands near 730 and 830 cm^{-1}. The intensity of these bands strongly increases when $x = 0.4$ and 0.8, and then decreases gradually for Ti^{4+}-rich compositions. As discussed previously, these bands can be attributed mainly to disorder-activated oxygen vibrations and a partial occupation of the 8a sites, which are completely empty in an ideal pyrochlore structure [13, 39]. Thus, our Raman results suggest that the $x = 0.4$ and 0.8 samples show the highest degree of oxygen disorder in this system, and that this disorder decreases for higher Ti^{4+} contents. These observations are in very good agreement with our own XRD data analysis shown before.

As for the $Gd_2Hf_{2-x}Sn_xO_7$ system, Fig. 4b shows that the Raman bands of $Gd_2Hf_2O_7$ also exhibit important shifts with increasing Sn^{4+} content (i.e., from 337, 412 and 543 cm^{-1} in $Gd_2Hf_2O_7$, to 309, 414 and 501 cm^{-1} for $Gd_2Sn_2O_7$). As in the $Gd_2Hf_{2-x}Ti_xO_7$ system, the intensity of the band near 602 cm^{-1} shows reduced intensity with increasing tin content and it is absent in $Gd_2Sn_2O_7$ (bottom spectrum). Furthermore, a new weak and narrow band appears at 533 cm^{-1}. This behavior strongly suggests that our previous assignment of the 602 cm^{-1} band in the $Gd_2Hf_{2-x}Ti_xO_7$ system to a F_{2g} mode [13] is probably not correct. Most likely, this F_{2g} mode in the Ti-containing system should be located near 530 cm^{-1} but it is obscured by the large width of the A_{1g} band; as this A_{1g} band is significantly narrower in the $Gd_2Hf_{2-x}Sn_xO_7$ system, the F_{2g} mode is clearly visible for samples with $x \geq 0.8$. Although the origin of the band near 600 cm^{-1} is not so clear, the fact that it exhibits decreasing intensity with increasing Ti^{4+} or Sn^{4+} content suggests that it should be related to oxygen disorder. Finally, for Sn-rich compositions ($x = 1.6$ and $x = 2$), the $Gd_2Hf_{2-x}Sn_xO_7$ system also shows an additional weak band at 345 cm^{-1}, not resolved for other chemical compositions, which can be attributed most likely to the E_g mode. As observed by XRD, this behavior supports the evolution of the $Gd_2Hf_{2-x}Sn_xO_7$ system into a very well-ordered pyrochlore structure, upon Sn^{4+} doping. In general, the Raman spectra of the $Gd_2Hf_{2-x}Sn_xO_7$ system show similar behavior as the Ti-containing system although the effects associated to higher structural

ordering, i.e., narrowing of Raman bands and increasing intensity of the A_{1g} band with lower Hf^{4+} content are much more pronounced.

Contrary to these two systems, $Gd_2Hf_{2-x}Sn_xO_7$ and $Gd_2Hf_{2-x}Ti_xO_7$, doping with Zr^{4+} ions has almost no effect on the Raman bands of $Gd_2Hf_2O_7$, i.e., the Raman spectra of $Gd_2Hf_2O_7$ and $Gd_2Zr_2O_7$ (top and bottom spectra in Fig. 4c) are very similar and unambiguously assigned to highly defective pyrochlore structures. Therefore, all Raman bands in the $Gd_2Hf_{2-x}Zr_xO_7$ solid solution remain very broad irrespective of the Hf^{4+}/Zr^{4+} ratio, which is consistent with the system maintaining a highly disordered pyrochlore-type structure as discussed in the previous section.

In summary, the Raman study shows clearly that oxygen disorder in the $Gd_2Hf_{2-x}B_xO_7$ title systems decreases with increasing Ti^{4+} or Sn^{4+} content, but remains largely unaffected when the replacing cation is Zr^{4+}.

Electrical properties

Figure 5a–d shows some representative examples of the electrical characterization carried out in the title samples. Hf^{4+} substitution has also a significant influence on density. When firing at the same temperature, Ti^{4+} produces samples with higher density (83–91%) than Zr^{4+} (77–90%) or Sn^{4+} (67–91%). Nevertheless, impedance spectroscopy which is the technique used to study the electrical properties of these materials allows separating individual contributions from different regions of a sample, and determine its intrinsic conductivity. Figure 5a shows the frequency and temperature dependence of the real component of the electrical conductivity of

Figure 5 a Frequency and temperature dependence of the real component of the electrical conductivity of $Gd_2Hf_{1.6}Sn_{0.4}O_7$, in a log–log representation. b Frequency and temperature dependence of the real component of the dielectric permittivity also in a log–log representation, for the same sample. c Complex impedance plot of the same sample (measuring temperature = 380 °C). d Temperature dependence of the bulk conductivity for the whole $Gd_2Hf_{2-x}Sn_xO_7$ system; dashed lines in these graphs are least squares best fits to an Arrhenius-type law.
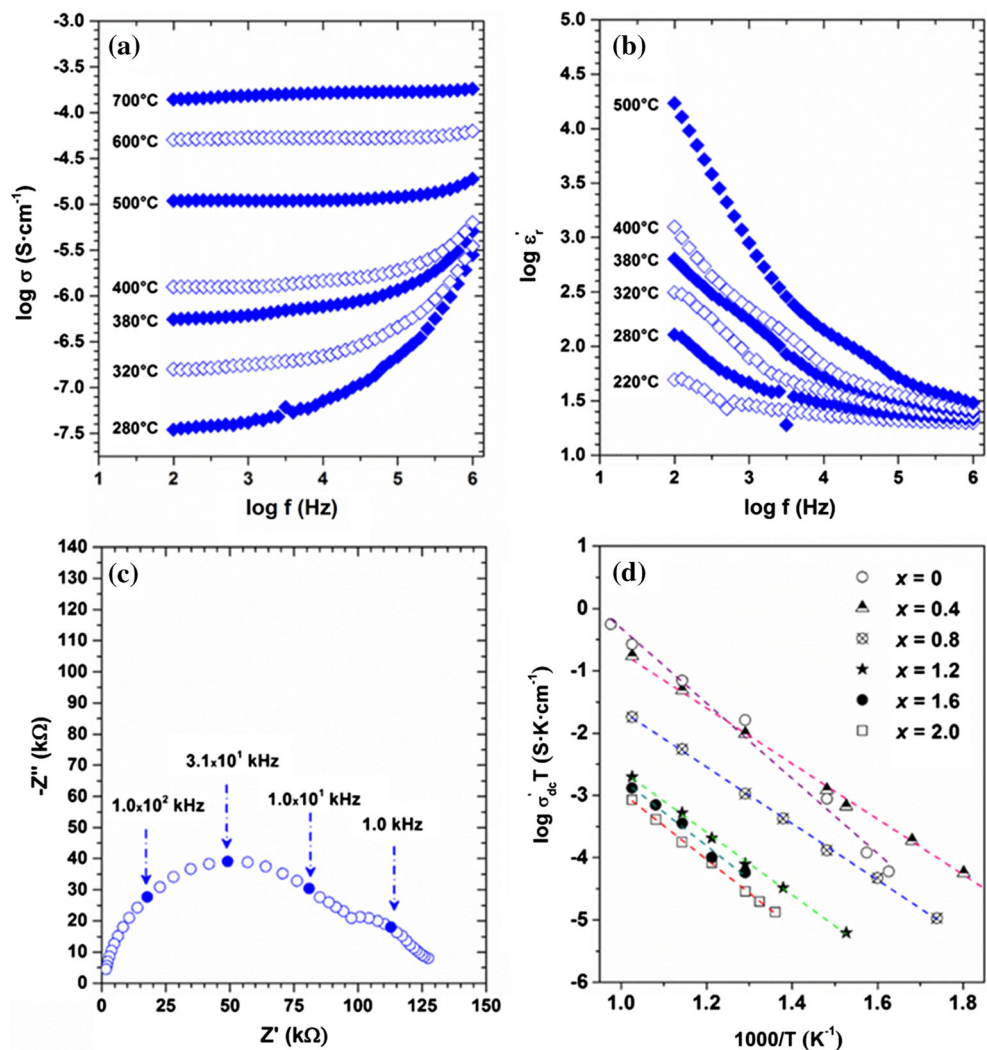
$Gd_2Hf_{1.6}Sn_{0.4}O_7$, in a log–log representation. Similar graphs were obtained for the remaining samples. Two different conductivity regimes are clearly observed in this graph; on the one hand, there is this region at low temperatures (e.g., ≤ 380 °C) and high frequencies, where conductivity shows a power-law type dependence with frequency, which has been linked to the hopping dynamics of mobile ions.

With increasing temperature, this region shifts to higher frequencies and out of the experimental window (≥ 500 °C). On the other hand, there is a plateau region at every temperature, where the conductivity is frequency independent; such regime which dominates this sample's response for measuring temperatures ≥ 500 °C is associated with the bulk conductivity, σ_{dc}. Figure 5b shows the frequency and temperature dependence of the real component of the dielectric permittivity also in a log–log representation, for the same sample. Ion blocking effects at grain boundaries and electrodes which are characteristic of ionic conduction are very much evident in this graph as significant increments in permittivity values shifting to higher frequencies with increasing temperature. Therefore, Fig. 5b confirms that conductivity in this system is mainly ionic. Figure 5c shows a complex impedance plot of the same sample (measuring temperature = 380 °C), which is similar to those characteristic of most solid electrolyte materials and features two semicircles, with capacitance values characteristic of grain boundary (low frequencies) and bulk contributions (high frequencies). Figure 5d shows the temperature dependence of the bulk conductivity for the whole $Gd_2Hf_{2-x}Sn_xO_7$ system; dashed lines in these graphs are least squares best fits to an Arrhenius-type law of the form of $\sigma_{dc}=(\sigma_0/T)\cdot\exp(-E_{dc}/kT)$, where E_{dc} is the activation energy for ion migration; σ_0 is the pre-exponential factor which is proportional to the number of mobile charge carriers in the structure; k is the Boltzmann constant and

T is the absolute temperature (K). This figure confirms that ion diffusion in the system is thermally activated. The activation energy (eV) as obtained from the slope of the Arrhenius graphs is shown in Table 6 and compared with that of the other two systems $Gd_2Hf_{2-x}Ti_xO_7$ and $Gd_2Hf_{2-x}Zr_xO_7$. Table 6 also shows the bulk conductivity of each composition, σ_{dc}, measured at 700 °C, whereas Fig. 6 depicts the effect of Hf^{4+} substitution by Ti^{4+} (Fig. 6a), Sn^{4+} (Fig. 6b) and Zr^{4+} (Fig. 6c), on the E_{dc} and $\log(\sigma T)_{700}$ of $Gd_2Hf_2O_7$.

Worth mentioning, E_{dc} and σ_{dc} values obtained in this work are comparable with those found in similar systems [40–42]. As observed in Table 6, the effect of Zr^{4+} is significantly different from that of Ti^{4+} and Sn^{4+}. Thus, σ_{dc} at 700 °C in the $Gd_2Hf_{2-x}Zr_xO_7$ series increases by almost an order of magnitude on increasing zirconium content (from 2.7×10^{-4} to 1.55×10^{-3} Sm cm^{-1}) whereas decreasing more than two orders of magnitude, when the replacing cation is either titanium (to 1.12×10^{-6} Sm cm^{-1}) or tin (to 8.71×10^{-7} Sm cm^{-1}). This effect is also graphically illustrated in the $\log(\sigma T)_{700}$ representation of Fig. 6 (red solid squares). It is noteworthy that the E_{dc} and σ_{dc} trends within each system are not correlated and lower E_{dc} does not necessarily render higher σ_{dc}. Thus, E_{dc} in the $Gd_2Hf_{2-x}Zr_xO_7$ system (6c) is hardly affected by substitution since both end limits display similar values (~ 1.2 eV); even though, the lowest E_{dc} value is obtained when $x = 0.8$ (1.035 eV). By contrast, the E_{dc} in the $Gd_2Hf_{2-x}Ti_xO_7$ system (6a) decreases almost continuously on increasing Ti content, reaching a minimum at $x = 1.6$ (0.716 eV) and then increasing again for $Gd_2Ti_2O_7$ (0.898 eV), whereas the E_{dc} in the $Gd_2Hf_{2-x}Sn_xO_7$ system (6b) decreases abruptly at first, reaching a minimum when $x = 0.4$ and then increases for higher Sn^{4+} contents ending at 1.07 eV for $Gd_2Sn_2O_7$. Finally, we found also of interest to plot in Fig. 6d the σ_{dc} versus

Table 6 E_{dc} and σ_{dc} (700 °C) for the three systems analyzed in this work

	$Gd_2Hf_{2-x}Ti_xO_7$		$Gd_2Hf_{2-x}Sn_xO_7$		$Gd_2Hf_{2-x}Zr_xO_7$	
	E_{dc} (eV)	σ_{dc} (Scm^{-1})	E_{dc} (eV)	σ_{dc} (Scm^{-1})	E_{dc} (eV)	σ_{dc} (Scm^{-1})
$x = 0.0$	1.194	2.70×10^{-4}	1.194	2.70×10^{-4}	1.194	2.70×10^{-4}
$x = 0.4$	0.964	4.78×10^{-4}	0.881	1.78×10^{-4}	1.126	1.09×10^{-3}
$x = 0.8$	1.057	6.61×10^{-5}	0.896	1.86×10^{-5}	1.035	1.25×10^{-3}
$x = 1.2$	0.741	3.02×10^{-6}	0.991	2.04×10^{-6}	1.116	1.48×10^{-3}
$x = 1.6$	0.716	3.46×10^{-6}	1.065	1.35×10^{-6}	1.162	1.58×10^{-3}
$x = 2.0$	0.898	1.12×10^{-6}	1.069	8.71×10^{-7}	1.176	1.55×10^{-3}

Figure 6 Effect of Hf^{4+} substitution by Ti^{4+} (**a**), Sn^{4+} (**b**) and Zr^{4+} (**c**), on the E_{dc} and $\log(\sigma T)_{700}$ of $Gd_2Hf_2O_7$; **d** σ_{dc} versus the cations size mismatch for the three systems.
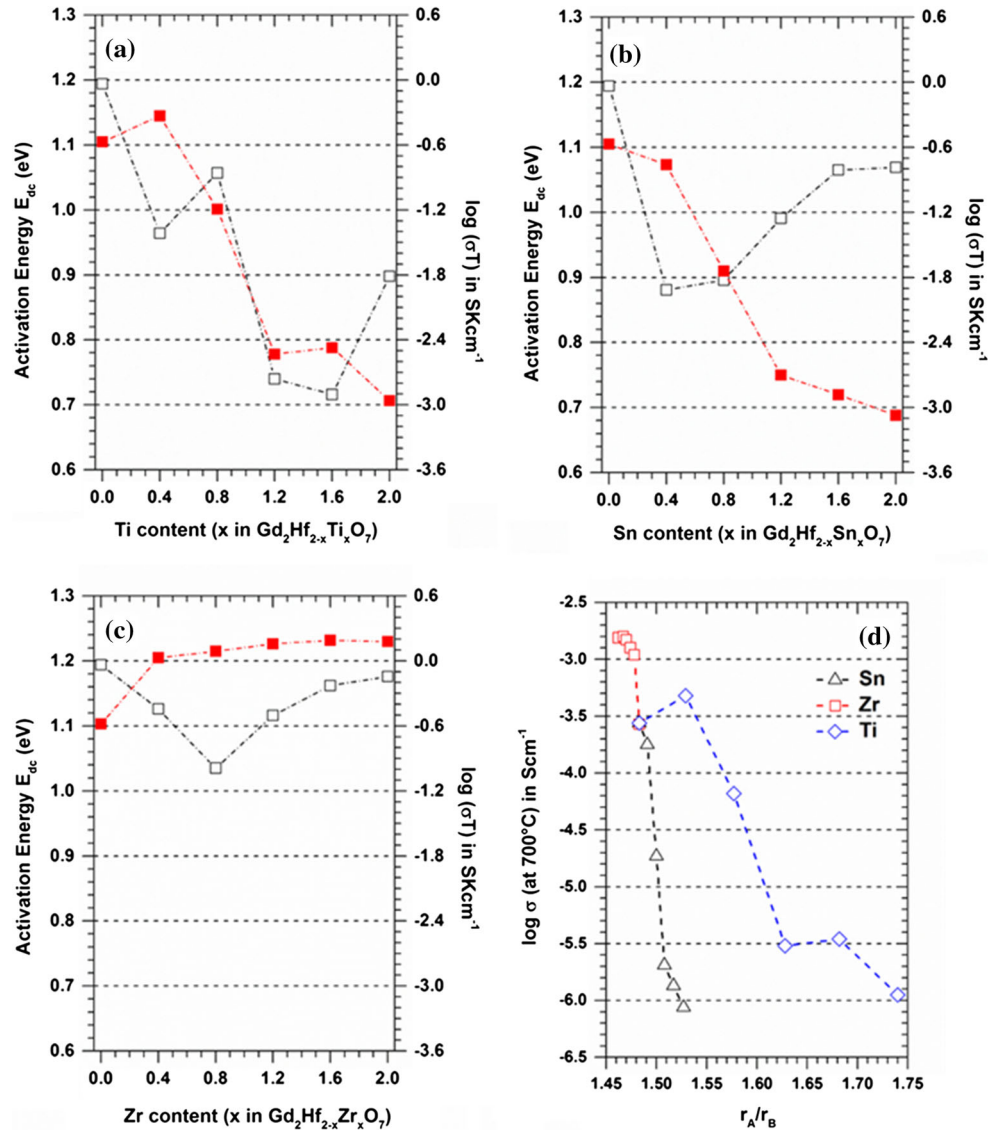
the cations size mismatch for the three systems. This graphs shows, indeed, that changes in the cations size ratio r_A/r_B cannot fully explain the trends in conductivity of these systems.

Worth mentioning, E_{dc} and σ_{dc} values obtained in this work are comparable with those found in similar systems [40–42]. As observed in Table 6, the effect of Zr^{4+} is significantly different from that of Ti^{4+} and Sn^{4+}. Thus, σ_{dc} at 700 °C in the $Gd_2Hf_{2-x}Zr_xO_7$ series increases by almost an order of magnitude on increasing zirconium content (from 2.7×10^{-4} to 1.55×10^{-3} Sm cm^{-1}) whereas decreasing more than two orders of magnitude, when the replacing cation is either titanium (to 1.12×10^{-6} Sm cm^{-1}) or tin (to 8.71×10^{-7} Sm cm^{-1}). This effect is also graphically

illustrated in the $\log(\sigma T)_{700}$ representation of Fig. 6 (red solid squares). It is noteworthy that the E_{dc} and σ_{dc} trends within each system are not correlated and lower E_{dc} does not necessarily render higher σ_{dc}. Thus, E_{dc} in the $Gd_2Hf_{2-x}Zr_xO_7$ system (6c) is hardly affected by substitution since both end limits display similar values (~ 1.2 eV); even though, the lowest E_{dc} value is obtained when $x = 0.8$ (1.035 eV). By contrast, the E_{dc} in the $Gd_2Hf_{2-x}Ti_xO_7$ system (6a) decreases almost continuously on increasing Ti content, reaching a minimum at $x = 1.6$ (0.716 eV) and then increasing again for $Gd_2Ti_2O_7$ (0.898 eV), whereas the E_{dc} in the $Gd_2Hf_{2-x}Sn_xO_7$ system (6b) decreases abruptly at first, reaching a minimum when $x = 0.4$ and then increases for higher Sn^{4+}

contents, ending at 1.07 eV for $Gd_2Sn_2O_7$. Finally, we found also of interest to plot in Fig. 6d the σ_{dc} versus the cations size mismatch for the three systems. This graphs shows, indeed, that changes in the cations size ratio r_A/r_B cannot fully explain the trends in conductivity of these systems.

Discussion

The most striking feature of the $A_2B_2O_7$ pyrochlore structure when compared to the ideal BO_2 fluorite structure is perhaps the fact that 1/8th of the anions are missing from the oxygen sublattice, i.e., as the stoichiometry changes from BO_2 to $A_2B_2O_7$, the anion-to-cation ratio decreases from 2 to 1.75, and anion vacancies are created to preserve electroneutrality. Using the Wyckoff's notation, such oxygen vacancies are ordered in the 8b site (3/8 3/8 3/8); interestingly, this site which is nominally empty in ideal (ordered) pyrochlore structures can be easily occupied by anions in defect (disordered) structures, mainly coming from the neighboring 48f site. On moving to the vacant 8b site, O_{48f} leave behind a continuous path for the migration of oxygen vacancies along the 48f position, transforming some defect pyrochlore-type oxides, into intrinsic oxygen ion conducting materials at high temperature. Correspondingly, the prevailing ion transport mechanism in this structure consists basically of consecutive 48f → 48f jumps along the <100> and <110> directions. Interestingly, anion disorder is favored by the presence of disorder also in the cation sublattice, which in turn, is mainly controlled by the A to B size mismatch, i.e., the r_A/r_B ratio. Another important factor determining the stability of the pyrochlore structure and its oxide ion conducting properties is the type (i.e., ionic vs. covalent) and strength of the metal–oxygen bonds, i.e., <A–O> but mostly, <B–O> bonds. Moreover, recent calculations have shown that migration along the <100> direction would be controlled by the strength of the <B–O> bond, whereas migration along the <110> direction would be governed by the size mismatch [43]. Our results confirm, indeed, that both characteristics are important when determining the electrical properties of $Gd_2Hf_2O_7$-based systems. The three substituting tetravalent cations selected for this study, Zr^{4+}, Sn^{4+} and Ti^{4+}, covered both factors; the first two have very similar ionic radii to Hf^{4+} although the <Sn–O>

bonding is significantly more covalent than <Zr–O> and <Hf–O>, whereas Ti^{4+} have a smaller ionic radius than Hf^{4+} and at the same time, its bonding to oxygen has a higher covalent contribution.

According to our structural study, all compositions prepared by mechanochemical synthesis in these three systems $Gd_2Hf_{2-x}B_xO_7$ (B = Ti, Sn, Zr) present an averaged pyrochlore-like structure after firing at 1500 °C, in agreement with the r_A/r_B size ratio criteria for pyrochlore stability, i.e., the pyrochlore structure is thermodynamically favored at room temperature, over the anion deficient fluorite structure in all four end members of the three systems targeted in the present study. As for the evolution of the unit cell size on substitution, Zr^{4+} and Sn^{4+} do not produce major changes since both have very similar ionic radii to Hf^{4+}. By contrast, the unit cell size decreases significantly when the substituting cation is Ti^{4+}. As for the degree of structural disorder, XRD results also show that cation distribution in $Gd_2Hf_{2-x}Zr_xO_7$ is highly disordered with a significant amount of Gd^{3+} ions (c.a. 25%) occupying the 16d octahedral site and correspondingly equal number of (Hf^{4+}/Zr^{4+}) ions located at the eightfold coordinated site. Therefore, both end members seem to present a highly disordered pyrochlore structure when obtained by mechanical milling, even after firing at 1500 °C and slow cooling to room temperature. Cation distribution in the $Gd_2Hf_{2-x}Sn_xO_7$ and $Gd_2Hf_{2-x}Ti_xO_7$ systems is another story. Therefore, the first one shows a continuous trend toward better ordered structures with increasing Sn^{4+} content and $Gd_2Sn_2O_7$ features an almost perfect pyrochlore structure, in agreement with previous studies [32]. Raman spectroscopy confirms the XRD analysis results and show that although the averaged structure in every case is of pyrochlore-type, each system shows a very different degree of oxygen disorder. Thus, disorder is high in $Gd_2Hf_2O_7$, decreases when the replacing cation is Sn^{4+} or Ti^{4+} but remains high when using Zr^{4+}. As for the electrical properties, we have also shown that in general both Sn^{4+} and Ti^{4+} substitutions have a detrimental effect in conductivity, whereas Zr^{4+} incorporation increases σ_{dc}, by almost half an order of magnitude. Nevertheless, the highest conductivity in the $Gd_2Hf_{2-x}Ti_xO_7$ system was obtained for $Gd_2Hf_{1.6}Ti_{0.4}O_7$. Changes in the size ratio cannot explain σ_{dc} values since change in it seems, however, to be correlated with decreasing covalency in the B^{4+}–O

bonds. The observed behavior cannot be related to change in the ionic radius of the B^{4+} ion.

Conclusions

We have successfully prepared at room temperature, highly refractory and pyrochlore-type HfO_2-based oxides, using a mechanochemical reaction and the corresponding elemental oxides as reagents. Our results have shown that milling for 30 h in a planetary ball mill is enough to obtain single-phase multicomponent oxides of general formula $Gd_2Hf_{2-x}B_xO_7$ (B = Ti, Sn, Zr) and with a fluorite-like structure. XRD analysis and Raman spectroscopy have also shown that all of them present a pyrochlore-like structure after firing at 1500 °C although with different degree of structural disorder. Thus, Hf^{4+} substitution by Sn^{4+} and Ti^{4+} produce better ordered pyrochlore oxides, whereas Zr^{4+} substitution does not have much influence in disorder. Impedance spectroscopy analysis have confirmed that composition in the $Gd_2Hf_{2-x}Zr_xO_7$ system is high-temperature oxygen ion conducting materials with conductivities in the order of 10^{-3} Scm^{-1} at 700 °C, whereas Sn^{4+} and Ti^{4+} substitutions have a detrimental effect in conductivity. Both, the cations size ratio r_A/r_B and the ionic/covalent character of the <B–O> bonding influence the structural characteristics and the electrical conductivity of these oxides.

Acknowledgements

Compliance with ethical standards

Conflict of interest The authors declare they have no conflict of interest.

References

[1] Subramanian MA, Aravamudan G, Rao GVS (1983) Oxide pyrochlores—a review. Prog Solid State Chem 15:55–143

[2] Darriet B, Rat M, Galy J, Hagenmuller P (1971) Sur quelques nouveaux pyrochlores des systemes MTO$_3$–WO$_3$ et MTO$_3$–TeO$_3$ (M = K, Rb, Cs, Tl; T = Nb, Ta). Mater Res Bull 6:1305–1316

[3] Jerez A, López ML, García-Martín S, Veiga ML, Pico C (1991) Defect pyrochlore structure A$_2$B$_2$X$_6$: a general approach to the coordination polyhedral around the metal ions. J Mater Sci 26:5163–5166. https://doi.org/10.1007/BF01143208

[4] Alonso JA, Castro A, Rasines I, Turrillas XM (1988) Study of the defect pyrochlores A(SbTe)O$_6$ (A = K, Rb, Cs, Tl). Mater Res Bull 23:4103–4107

[5] Hiroi Z, Yonezawa S, Nagao Y, Yamaura J (2007) Extremely strong-coupling superconductivity and anomalous lattice properties in the beta-pyrochlore oxide KOs$_2$O$_6$. Phys Rev B 76:014523

[6] Diaz-Guillen JA, Fuentes AF, Diaz-Guillen MR, Almanza JM, Santamaría J, Leon C (2009) The effect of homovalent A-site substitutions on the ionic conductivity of pyrochlore-type Gd$_2$Zr$_2$O$_7$. J Power Sources 186:349–352

[7] Tao S, Irvine JTS (2004) Discovery and characterization of novel oxide anodes for solid oxide fuel cells. Chem Rec 4:83–95

[8] Matsuhira K, Wakeshima M, Nakanishi R, Yamada T, Nakamura A, Kawano W, Takagi S, Hinatsu Y (2007) Metal-insulator transition in pyrochlore iridiates Ln$_2$Ir$_2$O$_7$ (Ln = Nd, Sm and Eu). J Phys Soc Jpn 76:043706

[9] Wuensch BJ, Eberman KW, Heremans C, Ku EM, Onnerud P, Yeo EME, Haile SM, Stalick JK, Jorgensen JD (2000) Connection between oxygen-ion conductivity of pyrochlore fuel-cell materials and structural change with composition and temperature. Solid State Ionics 129:111–133

[10] Wu J, Wei XZ, Padture NP, Klemens PG, Gell M, Garcia E, Miranzo P, Osendi M (2002) Low-thermal-conductivity rare-earth zirconates for potential thermal-barrier-coating applications. J Am Ceram Soc 85:3031–3035

[11] Ewing RC, Weber WJ, Lian J (2004) Nuclear waste disposal-pyrochlore A$_2$B$_2$O$_7$: nuclear waste form for the immobilization of plutonium and "minor" actinides. J Appl Phys 95:5949–5971

[12] López-Cota FA, Cepeda-Sánchez NM, Díaz-Guillén JA, Dura OJ, Maczka M, Ptak M, Fuentes AF (2017) Electrical and thermophysical properties of mechanochemically obtained lanthanide hafnates. J Am Ceram Soc 100:1994–2004

[13] Cepeda-Sánchez NM, Díaz-Guillén JA, Maczka M, Amador U, Fuentes AF (2017) Mechanochemical synthesis, crystal structure and ion conduction in the $Gd_2Hf_{2-x}Ti_xO_7$ system. J Mater Sci 52:11933–11946. https://doi.org/10.1007/s10853-017-1037-2

[14] Cepeda-Sánchez NM, Fuentes F, López-Cota FA, Rodrı́guez-Reyes M, Díaz-Guillén JA (2015) Mechanochemical synthesis and electrical properties of $Gd_2Hf_{2-x}Zr_xO_7$ solid electrolytes for their use in SOFC's. J Appl Electrochem 45:1231–1237

[15] Turner KM, Rittman DR, Heymach RA, Tracy CL, Turner ML, Fuentes AF, Mao WL, Ewing RC (2017) Pressure-induced structural modifications of rare-earth hafnate pyrochlore. J Phys Condens Matter 29:255401

[16] Chakoumakos BC (1984) Systematics of the pyrochlore structure type, ideal $A_2B_2X_6Y$. J Solid State Chem 53:120–129

[17] Brik MG, Srivastava AM (2012) Pyrochlore structural chemistry: predicting the lattice constant by the ionic radii and electronegativities of the constituent ions. J Am Ceram Soc 95:1454–1460

[18] Isupov VA (1958) Geometric criteria of structures of the pyrochlore type. Kristallografiya 3:99–100

[19] Suryanarayana C (2001) Mechanical alloying and milling. Prog Mater Sci 46:1–184

[20] Takacs L (2002) Self-sustaining reactions induced by ball milling. Prog Mater Sci 47:355–414

[21] Huot J, Liang G, Schulz R (2001) Mechanically alloyed metal hydride systems. Appl Phys A Mater Sci Process 72:187–195

[22] Fuentes AF, Takcs L (2013) Preparation of multicomponent oxides by mechanochemical methods. J Mater Sci 48:598–611. https://doi.org/10.1007/s10853-012-6909-x

[23] Rodriguez-Carvajal J (1993) Recent advances in magnetic structure determination by neutron powder diffraction. Physica B 192:55–69; See also a report in CPD of IUCr, Newsletter 2001, 26, 12; available at http://www.iucr.org/iucr-top/comm/cpd/Newsletters. The program and manual can be found at http://www-llb.cea.fr/fullweb/powder.htm

[24] Langford JI (1992) The use of the Voigt function in determining microstructural properties from diffraction data by means of pattern decomposition. In: Prince E, Stalick JK (eds) Proceedings of the international conference "Accuracy in Powder Diffraction II", NIST special publication 846, Gaithersburg, MD, USA, pp 110–126

[25] Langford JI (1999) Use of pattern decomposition or simulation to study microstructure: theoretical considerations. In: Snyder RL, Fiala J, Bunge HJ (eds) Defect and microstructure analysis by diffraction, IUCr monographs on

crystallography 10. Oxford University Press, Oxford, pp 59–81

[26] Louër D (1999) Use of pattern decomposition to study microstructure: practical aspects and applications. In: Snyder RL, Fiala J, Bunge HJ (eds) Defect and microstructure analysis by diffraction, IUCr monographs on crystallography 10. Oxford University Press, Oxford, pp 671–697

[27] Halder NC, Wagner CNJ (1966) Analysis of the broadening of powder pattern peaks using variance, integral breadth, and Fourier coefficients on the line profile. Adv X-Ray Anal 9:91–102

[28] Michel D, Mazerolles L, Berthet P, Gaffet E (1995) Nanocrystalline and amorphous oxide powders prepared by high-energy ball-milling. Eur J Solid State Inorg Chem 32:673–682

[29] Heremans C, Buensch WJ, Stalick JK, Prince E (1995) Fast-ion conducting $Y_2(Zr_yTi_{1-y})_2O_7$ pyrochlores: neutron Rietveld analysis of disorder induced by Zr substitution. J Solid State Chem 117:108–121

[30] Moreno KJ, Fuentes AF, Maczka M, Hanuza J, Amador U (2006) Structural manipulation of pyrochlores: thermal evolution of metastable $Gd_2(Ti_{1-y}Zr_y)_2O_7$ powders prepared by mechanical milling. J Solid State Chem 179:3805–3813

[31] Shannon RD (1976) Revised effective ionic radii and systematic studies of interatomic distances in halides and chalcogenides. Acta Cryst A32:751–767

[32] Kennedy BJ, Hunter BA, Howard CJ (1997) Structural and bonding trends in tin pyrochlore oxides. J Solid State Chem 130:58–65

[33] Reyes M, Whittle KR, Zhang Z, Ashbrook SE, Mitchell MR, Jang LY, Lumpkin GR (2013) The pyrochlore to defect fluorite phase transition in $Y_2Sn_{2-x}Zr_xO_7$. RSC Adv 3:5090–5099

[34] Moreno KJ, Fuentes AF, Maczka M, Hanuza J, Amador U, Santamaría J, León C (2007) Influence of thermally induced oxygen order on mobile ion dynamics in $Gd_2(Ti_{0.65}Zr_{0.35})_2O_7$. Phys Rev B 75:184303

[35] Fuentes AF, Boulahya K, Maczka M, Hanuza J, Amador U (2005) Synthesis of disordered pyrochlores, $A_2Ti_2O_7$ (A = Y, Gd and Dy), by mechanical milling of constituent oxides. Solid State Sci 7:343–353

[36] Maczka M, Hanuza J, Hermanowicz K, Fuentes AF, Matsuhira K, Hiroi ZJ (2008) Temperature-dependent Raman scattering studies of the geometrically frustrated $Dy_2Ti_2O_7$, $Gd_2Ti_2O_7$ and $Er_2Ti_2O_7$. J Raman Spectrosc 39:537–544

[37] Garg N, Pandey KK, Murli C, Shanavas KV, Mandal BP, Tyagi AK, Sharma SM (2008) Decomposition of lanthanum hafnate at high pressures. Phys Rev B 77:214105

[38] Glerup M, Nielsen OF, Poulsen FW (2001) The structural transformation from the pyrochlore structure, $A_2B_2O_7$, to the

fluorite structure, AO_2, studied by Raman spectroscopy and defect chemistry modeling. J Solid State Chem 160:25–32

[39] Sanjuán ML, Guglieri C, Diaz-Moreno S, Aquilanti G, Fuentes AF, Olivi L, Chaboy J (2011) Raman and x-ray absorption spectroscopy of the phase evolution induced by mechanical milling and thermal treatments in $R_2Ti_2O_7$ pyrochlores. Phys Rev B 84:104207

[40] Shlyakhtina AV, Knotko AV, Boguslavskii MV, Stefanovich SYu, Kolbanev IV, Larina LL, Shcherbakova LG (2007) Effect of non-stoichiometry and synthesis temperature on the structural and conductivity of $Ln_{2+x}M_{2-x}O_{7-x/2}$ (Ln = Sm-Gd; M = Zr, Hf; x = 0–0.286). Solid State Ionics 178:59–66

[41] Shlyakhtina AV, Shcherbakova LG (2011) Polymorphism and high-temperature conductivity of $Ln_2M_2O_7$ (Ln = Sm–Lu; M = Ti, Zr, Hf) pyrochlores. Solid State Ionics 192:200–204

[42] Shlyakhtina AV, Shcherbakova LG (2012) New solid electrolytes of the pyrochlore family. Russ J Electrochem 48:3–30

[43] Nakamura K, Mori M, Itoh T, Ohnuma T (2016) Theoretical and experimental investigation of defect formation/migration in $Gd_2Ti_2O_7$: general rule of oxide-ion migration in $A_2B_2O_7$ pyrochlore. AIP Adv 8:115003